Determination of anisotropic optical properties of MOCVD grown m-plane α-$(Al_xGa_{1-x})_2O_3$ alloys

Elias Kluth,[1, a)] A F M Anhar Uddin Bhuiyan,[2] Lingyu Meng,[2] Jürgen Bläsing,[1] Hongping Zhao,[2, 3] Rüdiger Goldhahn,[1] and Martin Feneberg[1]

[1)] *Institut für Physik, Otto-von-Guericke-Universität Magdeburg, Universitätsplatz 2, 39106 Magdeburg, Germany*
[2)] *Department of Electrical and Computer Engineering, The Ohio State University, Columbus, Ohio, USA*
[3)] *Department of Materials Science and Engineering, The Ohio State University, Columbus, Ohio, USA*

(Dated: 27 February 2023)

The anisotropic dielectric functions (DF) of corundum structured m-plane α-$(Al_x Ga_{1-x})_2O_3$ thin films (up to x=0.76) grown on m-plane sapphire substrate by metal-organic chemical vapour deposition have been investigated. Infrared (IR), and visible-ultraviolet (UV) spectroscopic ellipsometry yield the DFs, while x-ray diffraction revealed the lattice parameters (a, m, c), showing the samples are almost fully relaxed. Analysis of the IR DFs from 250cm^{-1} to 6000cm^{-1} by a complex Lorentz oscillator model yields the anisotropic IR active phonons E_u & A_{2u} and the shift towards higher wavenumbers with increasing Al content. Analyzing the UV DFs from 0.5 to 6.6eV we find the change in the dielectric limits ε_∞ and the shift of the Γ-point transition energies with increasing Al content. This yields anisotropic bowing parameters for α-$(Al_x Ga_{1-x})_2O_3$ of $b_\perp$=2.1eV and $b_{||}$=1.7eV.

I. INTRODUCTION

Ga_2O_3, in all polymorphs (α, β, γ, δ, ϵ, κ), is an ultra wide bandgap semiconductor.[1,2] Hence, it also has a very high electric breakdown field.[3] Consequently, it is of increasing interest,[4] due to its possibilities of application in high power electronics e.g. field-effect transistors like MOSFETs or MESFETs.[5,6] Additionally, applications in optical devices like solar-blind photodetectors[2,5,7] or solar cells[8–10] are possible.

Most intensely investigated, is certainly the thermodynamically stable monoclinic β-phase ($C2/m$). Furthermore, with the γ-phase($Fd\bar{3}m$) (just recently explored in greater detail by Ratcliff *et al.*[11]) and the δ-phase ($Ia\bar{3}$) there are two cubic polymorphs, along with the two orthorhombic polymorphs ϵ- ($P6_3mc$) and κ-phase ($Pna2_1$) [ref]. The last of the six polymorphs of Ga_2O_3 is the rhombohedral corundum- structured α-phase ($R\bar{3}c$).[2]

The benefits of the metastable α-phase are the possibility of growth using sapphire (α-Al_2O_3) as an affordable substrate with the same crystal structure, a higher symmetry and a slightly higher bandgap[12–16] compared to β-Ga_2O_3. Also α-Ga_2O_3 offers the possibility of alloying with other group III elements like In or Al. In_2O_3, despite having a stable cubic bixbyite phase ($Ia\bar{3}$),[17] as well has a metastable corundum crystal structure.[18] This offers the opportunity of bandgap engineering over the wide range from 3.38eV (α-In_2O_3)[18] to 9.2eV (α-Al_2O_3).[19] This paves the way into the ultra violet spectral range, further than the $(Al_xGa1_{-x})N$ system does (AlN E_g=5.96eV[20]), where already high electron mobility transistors,[21] laser diodes,[22,23] or solar-blind photodetectors[24] have been realized.

Some attempts to alloy the stable β-Ga_2O_3 phase with Al have been made,[25–27] but this remains challenging since α-Al_2O_3 does not share the same crystal structure and monoclinic Al_2O_3 (θ-Al_2O_3) remains obscure.[28] In contrast alloying α-Ga_2O_3 with Al can provide single-crystal films by chemical vapour deposition (CVD),[29] pulsed laser deposition (PLD),[30] and molecular beam epitaxy (MBE),[31] especially when grown on m-plane sapphire.[32] c-plane Al_2O_3 as substrate seems to lead to the formation of a few monolayers α-Ga_2O_3 followed by β-Ga_2O_3, due to the large in-plane lattice mismatch between layer and substrate, independent of the growth method.[32,33] This is not the case for m-plane Al_2O_3 substrates, where much thicker single phase α-Ga_2O_3 layers have been observed.[34] Also, first attempts of doping α-Ga_2O_3,[35,36] α-Al_2O_3,[37] and the α-$(Al_x Ga_{1-x})_2O_3$ alloy system[38] have been made. Sn doping of α-Ga_2O_3 on m-plane Al_2O_3 showed mobilities much higher than films grown on c-plane Al_2O_3.[39] The increasing interest in technical applications is even mirrored by DFT calculations[40] e.g. on the possibilities of donor doping α-$(Al_xGa_{1-x})_2O_3$ by different dopants.[41]

So far, some investigations of the optical properties of α-$(Al_x Ga_{1-x})_2O_3$ have been made by Ito *et al.*[42] and Jinno *et al.*[32] employing transmission measurements. Dang *et al.*[29] analyzed a Tauc plot and Uchida *et al.*,[43] Chen *et al.*,[30] and Xia *et al.*[44] utilized x-ray photoelectron spectroscopy to determine bandgap values and/or bowing parameters. But since the corundum crystal structure is anisotropic, a polarization dependent investigation of the material properties is crucial. Studies of the optical properties of α-$(Al_xGa_{1-x})_2O_3$ taking into account the anisotropy are rare. Hilfiker *et al.* investigated the optical absorption onset[28] and dielectric limits ε_∞[45] by spectroscopic ellipsometry. Additionally Stokey *et al.*[46] determined infrared-active phonon modes and static dielectric constants with the same technique in the infrared. Their results will be compared to our results in

[a)]Electronic mail: elias.kluth@ovgu.de

more detail below.

m-plane α-$(Al_xGa_{1-x})_2O_3$ thin films up to x=0.76 grown by metal-organic chemical vapour deposition (MOCVD) on m-plane sapphire substrate have been investigated anisotropically. X-ray diffraction, yields lattice parameters while infrared (IR) & visible-ultraviolet (UV) spectroscopic ellipsometry, yield the complex dielectric functions (DF) in both spectral ranges. The IR DF is dominated by the IR active phonons. The UV DF yields the dielectric limit ε_∞ and the Γ-point transition energies. They are in turn used to determine the anisotropic bowing parameters.

II. EXPERIMENTAL

α-$(Al_xGa_{1-x})_2O_3$ thin films (~100nm) were grown by MOCVD on m-plane sapphire substrates using a MOCVD reactor (Agitron Agilis). The precursors used were trimethylaluminum (TMAl), triethylgallium (TEGa), and pure O_2, while Ar was the carrier gas. Beforehand, the substrates were cleaned *ex situ* with solvents and *in situ* in the reaction chamber by high temperature cleaning at 920° C under O_2 atmosphere. Afterwards the epitaxial growth was initiated in a temperature range of 650-880° C and a pressure of 20 to 80 Torr. Details on the growth process,

as well as comprehensive material characterization e.g. RSM, AFM, Raman spectroscopy, XPS, HAADF-STEM, and EDS, can be found elsewhere.[47]

Crystal quality and the lattice parameters of the samples were determined by X-ray diffraction (XRD) measurements. The in-plane c and a values and their full width at half maximum (FWHM) were directly quantified by Grazing Incidence In-plane Diffraction (GIID) at the critical angle of incidence of 0.36° (for Cu-Kα radiation the 2θ angles were at 36.1° (x=0) for $(11\bar{2}0)$, and at 40.15° (x=0) for (0006)) (Seifert/ FPM URD6/GIID). The m values were determined by High-Resolution X-Ray Diffraction (HRXRD) on (3030) using Cu-Kα at 64.8° (x=0) (Rigaku SL μHR).

Values of Ga_2O_3 by Marezio *et al.*[48] and Al_2O_3 by Leszczynski *et al.*[49] were used to apply Vegard's law[50] to the measured lattice parameters:

$$a_{AlGa_2O_3} = x\, a_{Al_2O_3} + (1-x)\, a_{Ga_2O_3} \quad (1)$$

Generalized[51] IR spectroscopic ellipsometry was performed using a Fourier-transform ellipsometer (Woollam IR-VASE) in the range of 250cm^{-1} to 6000cm^{-1} with the resolution set to 4cm^{-1}. The measurements were carried out at three angles of incidence Φ of 50°, 60°, and 70°. In generalized spectroscopic ellipsometry, three ratios of the complex reflection coefficients are measured, r_{pp}/r_{ss}, r_{ps}/r_{pp}, and r_{sp}/r_{ss}, which then provide the corresponding ellipsometric angles Ψ and Δ,[52] where Ψ is the amplitude ratio between the parallel and the perpendicular polarization orientation of the reflected light from the sample, with respect to the plane of incidence, and Δ is the phase shift between them. Ψ and Δ can be transformed into the complex refractive index ρ:

$$\rho = \tan(\Psi) e^{i\Delta}. \quad (2)$$

From that, the pseudo DF can be calculated as

$$\langle \varepsilon \rangle = \sin^2(\Phi)\left(\tan^2(\Phi)\left(\frac{1-\rho}{1+\rho}\right)^2\right). \quad (3)$$

In an isotropic sample, with only one semi-infinite layer the pseudo DF is identical to the actual DF of the material. In any other case, e.g in case of thin film samples, the pseudo DF is only the DF of the sample and a multi-layer model has to be used and fitted to disentangle the DF of the layer of interest. Here, the model contains two layers, the sapphire substrate, based on measurements of a m-plane sapphire wafer, and the α-$(Al_xGa_{1-x})_2O_3$ layer of interest. Since both, α-$(Al_xGa_{1-x})_2O_3$ and the underlying m-plane sapphire are anisotropic crystals in corundum structure, each sample must be measured twice, with the c-axis perpendicular and parallel to the plane of incidence. From this we gain the ordinary DF ($\varepsilon_\perp$) with the electric filed vector $\mathbf{E}\perp\mathbf{c}$ and the extraordinary DF ($\varepsilon_{||}$) with $\mathbf{E}||\mathbf{c}$. The model dielectric functions in the region of the IR active phonons, contain a dielectric background ε_∞ and a sum of Lorentzian broadened phonon oscillators, with the phonon frequency ω_{TO}, the broadening parameter γ_{TO} and the Amplitude S:

$$\varepsilon_\perp(\omega) = \varepsilon_{\infty,\perp} + \sum_{l=1}^{4} \frac{S_l \omega_{TO,l}^2}{\omega_{TO,l}^2 - \omega^2 - i\gamma_{TO,l}\omega} \quad (4)$$

$$\varepsilon_{||}(\omega) = \varepsilon_{\infty,||} + \sum_{k=1}^{2} \frac{S_k \omega_{TO,k}^2}{\omega_{TO,k}^2 - \omega^2 - i\gamma_{TO,k}\omega} \quad (5)$$

with 6 IR active phonons in the rhombohedral corundum structure:

$$\Gamma_{opt,\,IR} = 4E_u + 2A_{2u} \quad (6)$$

4 E_u in $\varepsilon_\perp$ and 2 A_{2u} in $\varepsilon_{||}$.[53] This anisotropic multi-layer model is used as a starting-point for a point-by-point (pbp) fit, where the model is fitted numerically to the experimental data at every wavenumber until the best match is obtained. This leads to the final dielectric functions. In a last step, these numerical dielectric functions were fitted with their model DFs (Eq. (4 & 5)) to determine parameters like the phonon wavenumber.

Generalized UV spectroscopic ellipsometry was performed with a variable-angle scanning ellipsometer based on a grating monochromator, equipped with an autoretarder, in the range from 0.5eV (4000cm^{-1}) to 6.6eV, thus it overlaps with the IR ellipsometry range. Identical to the IR ellipsometry the UV ellipsometry measures three ratios of the complex reflection coefficients, which yield corresponding ellipsometric angles Ψ and Δ. Furthermore in the UV as well, measurements were taken twice to determine both, $\varepsilon_\perp$ and $\varepsilon_{||}$. However, in the UV range a surface roughness has to be taken into account for the multi-layer model using an effective medium approximated layer (EMA) with Bruggeman's formalism.[54] The underlying m-plane sapphire is modeled with a model DF from Malitson.[55] By modeling

for the Fabry-Pérot oscillations the thickness of the epitaxial layer can be determined (see Tab. I). The α-$(Al_xGa_{1-x})_2O_3$ layer of interest is modeled anisotropically using a general oscillator model containing the Herzinger-Johs parameterized semiconductor oscillator functions (PSEMI) to describe the line-shape of the experimental results[56,57] based on an anisotropic model for r-plane α-Ga_2O_3 by Kracht *et al.*[14] Again consistent with the evaluation of the IR ellipsometry, in the UV, this multi-layer model is used as starting point for a point-by-point fit yielding the actual dielectric functions. In the region below the first transition energy (0.5eV - 5eV) the real part of the DF, which corresponds to the square of the refractive index (while the imaginary part which corresponds to the absorption coefficient is still zero) was fitted by a model from Shokhovets *et al.*:[58]

$$\varepsilon_1(\hbar\omega) = 1 + \frac{2}{\pi}\left(\frac{A_g}{2}\ln\left|\frac{E_H^2-(\hbar\omega)^2}{E_G^2-(\hbar\omega)^2}\right| + \frac{A_H E_H}{E_H^2-(\hbar\omega)^2}\right) \quad (7)$$

which allows the calculation of the dielectric limit ε_∞ :

$$\varepsilon_\infty = 1 + \frac{2}{\pi}\left(A_G \ln\left|\frac{E_H}{E_G}\right| + \frac{A_H}{E_H}\right) \quad (8)$$

In the region of the absorption onset, the dielectric functions were fitted to an error function-like shaped model DF in the imaginary part and the corresponding real part is based on a Kramers-Kronig transformation, using the earlier mentioned PSEMI functions, to determine the Γ-point transition energies E_{CV} of α-$(Al_xGa_{1-x})_2O_3$. We then use results from Kracht *et al.*[14] as fixed parameters of the transition energies and analyze the relative shift with Al content. This is discussed in more detail below (sec. III C). At last, an anisotropic bowing model is used to describe the change of the dielectric limit and the transition energy with increasing Al content *x*:

$$E_{CV\perp,||}(x) = (1-x)\,E_{Ga_2O_3\perp,||} + xE_{Al_2O_3\perp,||} - b_{\perp,||}\,x(1-x). \quad (9)$$

III. RESULTS AND DISCUSSION

A. XRD

Results of the XRD measurements, in terms of lattice parameters *a*, *m*, and *c* together with the FWHM of the $(30\bar{3}0)$, the $(11\bar{2}0)$, and the (0006) peak are displayed in Tab. I. There is an excellent agreement of the lattice parameters with previous results on m-plane Ga_2O_3.[59] The change in the lattice parameters with increasing Al content is displayed in Fig. 1 added by Vegard's law based on Eq. (1). *m* shows the best match with Vegard's law, which isn't surprising since the (3030) was used to determine the Al content, as discussed by Bhuiyan *et al.*[47] $m_a = a/\sqrt{(4/3)}$ matches well with Vegard's law, just *c* shows slight deviations. Note, that the deviations between *m* (blue) and m_a (red) show the fulfillment of the $m/a = \sqrt{3}/4$ relation. Overall, since the m_a values match the *m* values nicely and besides slight deviations all lattice parameters follow Vegard's law as well, all samples are almost fully relaxed.

TABLE I. Al contents (*x*), lattice parameters (*a*, *m* & *c*) and FWHM by Grazing Incidence In-plane Diffraction (GIID) and High Resolution X-ray Diffraction (HRXRD), together with thicknesses (*d*) by ultraviolet spectroscopic ellipsometry (UVSE) for all investigated α-$(Al_xGa_{1-x})_2O_3$ samples are listed, along with literature data on Ga_2O_3 powders,[48] c-plane Ga_2O_3,[15] m-plane Ga_2O_3,[59] and c- plane Al_2O_3.[49] Since Marezio *et al.*,[48] Ning *et al.*[15] and Leszczynski *et al.*[49] do not provide data on the *m*_value, we assumed fully relaxed samples and estimated *m* by $a/\sqrt{(4/3)}$. This values are printed *italic*.

x	*d*	*a*	*m*	*c*	FWHM $(30\bar{3}0)$	FWHM $(11\bar{2}0)$	FWHM (0006)
	nm	Å			arcsec		
0[a]	-	4.9825	*4.3150*	13.433	-	-	-
0[b]	800	4.9882	*4.3199*	13.4262	-	1430	83
0[c]	880	4.975	4.314	13.457	1033	1480	1537
0	89	4.9752	4.3119	13.4610	2304	3024	2988
0.07	101	4.9590	4.3005	13.4292	1440	1332	1332
0.15	101	4.9434	4.2822	13.4016	1296	1476	1512
0.26	121	4.9230	4.2615	13.3578	1116	1548	1620
0.36	119	4.9058	4.2450	13.3362	1152	1764	1800
0.76	202	4.8158	4.1676	-	864	1440	-
1[d]	-	4.7577	*4.1203*	12.9907	-	-	-

[a] Reference [48]
[b] Reference [15]
[c] Reference [59]
[d] Reference [49]

B. IR-Ellipsometry

For the *x*=0.07 α-$(Al_xGa_{1-x})_2O_3$ sample the experimental data (Ψ and Δ) are displayed in the region of the IR active phonon modes (250-600cm^{-1}) in comparison to the pbp-fit for the two measurements with the c-axis parallel and perpendicular to the plane of incidence in Fig. 2. The fit matches the data almost perfectly. This is exemplary for all samples.

Based on the pbp-fit, we obtain, the IR pbp-DFs displayed for the *x*=0.07 sample in Fig. 3, with $\varepsilon_\perp$ in the bottom and $\varepsilon_{||}$ in the top panel. Eq. (4) and (5) are used to fit these pbp-DFs and four out of the allowed six IR active phonon modes (Eq. (6)) could be determined for all samples. The missing phonon $E_u(1)$ is expected below the experimentally accessible spectral range starting at 250cm^{-1} for all samples till $x \approx 0.26$.[46] The fact that it is not found for higher Al concentrations either, is probably related to its comparatively low amplitude. For the same reason, the $E_u(4)$ is only found in the 0.76 sample. Noisy features between 350 and 450cm^{-1} are interpreted as artifacts and not considered further.

The characteristic wavenumbers (ω_0) of all phonon modes are listed in Tab. II, supplemented by data of a m-plane sap-

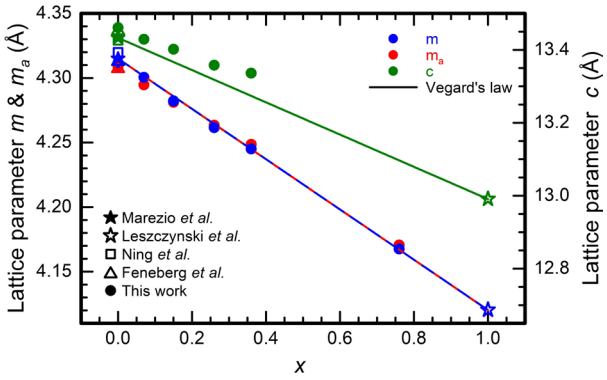

FIG. 1. Lattice parameters m (blue), $m_a = a/\sqrt{(4/3)}$ (red), and c (green) for different Al contents x for all m-plane α-$(Al_xGa_{1-x})_2O_3$ samples supplemented by literature data on Ga_2O_3 powders by Marezio *et al.*[48] c-plane Ga_2O_3, by Ning *et al.*,[15] m-plane Ga_2O_3 by Feneberg *et al.*[59] and c-plane Al_2O_3 by Leszczynski *et al.*[49] Vegard's law is added in the form of a linear interpolation between Ga_2O_3 data by Marezio *et al.*[48] and Al_2O_3 by Leszczynski *et al.*[49] See also Tab. I.

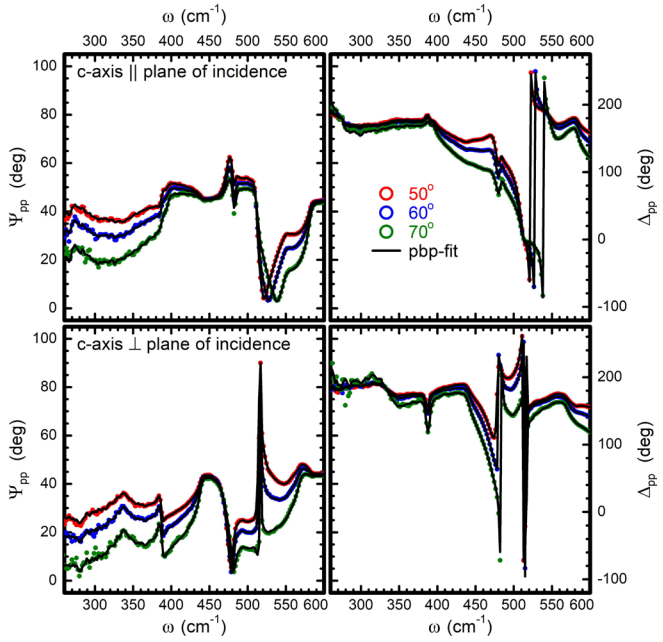

FIG. 2. Ellipsometric angles Ψ_{pp} (Left) and Δ_{pp} (right) of α-$(Al_xGa_{1-x})_2O_3$ for x=0.07 in the spectral range of the infrared-active optical phonons with the c-axis perpendicular to the plane of incidence (bottom) and parallel to the plane of incidence (top) for three different angles of incidence 50°, 60°, and 70° in red, blue, and green respectively, together with their corresponding point-by-point (pbp) fit in black.

phire wafer. They are listed in comparison to earlier studies and further literature on Ga_2O_3 and Al_2O_3, to which both, the results on Ga_2O_3 and Al_2O_3 are in a very satisfactory agreement.[13,15,59–61] Additionally, the results are displayed in Fig. 4, with the E_u (**E**⊥**c**) phonon modes in red and the A_{2u} (**E**||**c**) ones in green. The phonon modes follow approximately a linear trend, except the lower wavenumber phonons A_{2u} (1) and E_u (2). For comparison the values of Stokey *et al.*[46,60] on m-plane α-Ga_2O_3 & α-$(Al_xGa_{1-x})_2O_3$ PAMBE samples and Schubert *et al.*[61] on a- and c-plane Al_2O_3 are shown in the same Fig. as well. Unfortunately, there[46] no pbp-DFs but only model DFs were shown, therefore a comparison on this level is not possible. Also, a product ansatz was used instead of the sum ansatz used here (Eq. (4 & 5)), which, due to too many free parameters, often provides poorer results. Additionally the values of Tab. 1 and Fig. 3 (shown here) in Stokey *et al.*[46] do not align, which leads to confusion on the actually values. Overall, however their values fit to our results in most cases. Only the E_u (2) and the E_u (3) mode show slight deviations.

C. UV-Ellipsometry

Experimental results (Ψ & Δ) exemplary from the x=0.26 sample in the UV spectral range are shown in Fig. 5 with the corresponding pbp-fit for two different measurements one with the c-axis parallel and one perpendicular to the plane of incidence. The pbp-fit matches the data here as well almost perfectly.

The so obtained pbp-DFs are displayed in Fig. 6 for both $\varepsilon_{\perp}$ (solid) and $\varepsilon_{||}$ (dashed) with the real part ε_1 on the left and the imaginary part ε_2 on the right axis in the region around the absorption onset. Note that in the UV spectral range we do not provide DFs of α-Ga_2O_3 (i.e. x=0) in this work, but rather use established and already published anisotropic DFs from earlier studies by Kracht *et al.*[14]

The difference in line shape for $\varepsilon_{||}$ compared to $\varepsilon_{\perp}$ at the absorption onset is clearly visible together with a strong red shift of the absorption onsets with increasing Al content.

In the region of photon energies lower than the absorption onset, the real part of the dielectric functions was fitted using the model from Shokhovets *et al.*[58] and therefore an analytical expression of the refractive index is obtained (see supplement, Fig. S1). Using Eq. (8) the dielectric limit ε_∞ can be determined from the fitted values E_G, A_G, E_H, and A_H.

The trend of the dielectric limit as a function of Al content x is displayed in Fig. 7 (red & green circles) and compared to results of Hilfiker *et al.*[45] (black & gray triangles) and their corresponding bowing fit (black & gray dashed lines).

Overall, the results of Hilfiker *et al.*[45] match well with our results here. ($\varepsilon_{\infty,\perp}$ is always higher than $\varepsilon_{\infty,||}$. Only for the x=0.07 sample, slight deviations are obvious, but we assign this to imperfect fitting of the Shokhovets model to the pbp- DF due to artifacts in the dielectric function caused by an imperfect point-by-point fit in this spectral range (~2-4eV). In the next step, we now analyze the UV DF in the region of the absorption onsets to obtain the Γ-point transition energies $E_{CV,}$ whereby $E_{CV,\perp}$ corresponds to Γ_{1-1}+Γ_{1-2},[16] and $E_{CV,||}$ to Γ_{1-3}.[16] First of all, we note, that Kracht *et al.*[14] and Hilfiker *et al.*[16,28] agree on the line shape of the DF. However, their analysis of these DFs yield very different re-

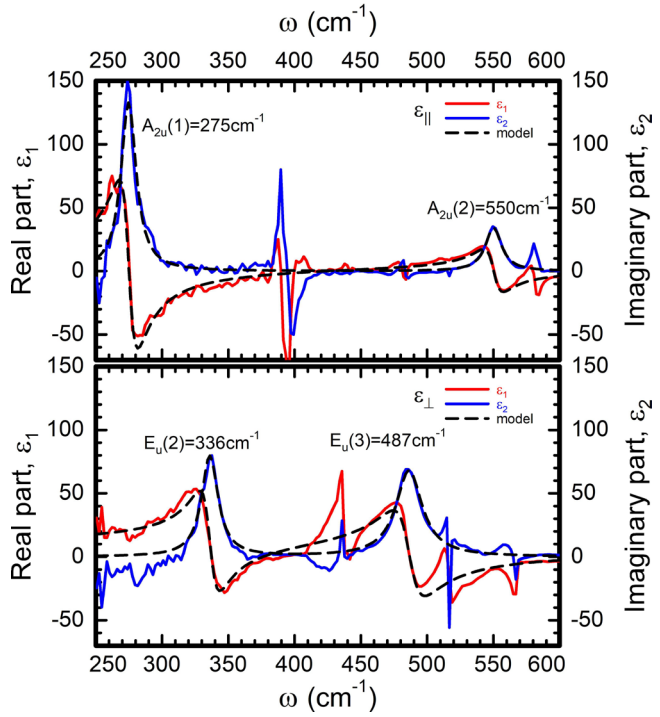

FIG. 3. Point-by-Point complex dielectric functions with real and imaginary parts (red & blue) of α-$(Al_xGa_{1-x})_2O_3$ for x=0.07, and line-shape models (black) in the spectral range of infrared-active optical phonons, with $\boldsymbol{\varepsilon}_{\perp}$ in the bottom panel and $\boldsymbol{\varepsilon}_{||}$ in the top.

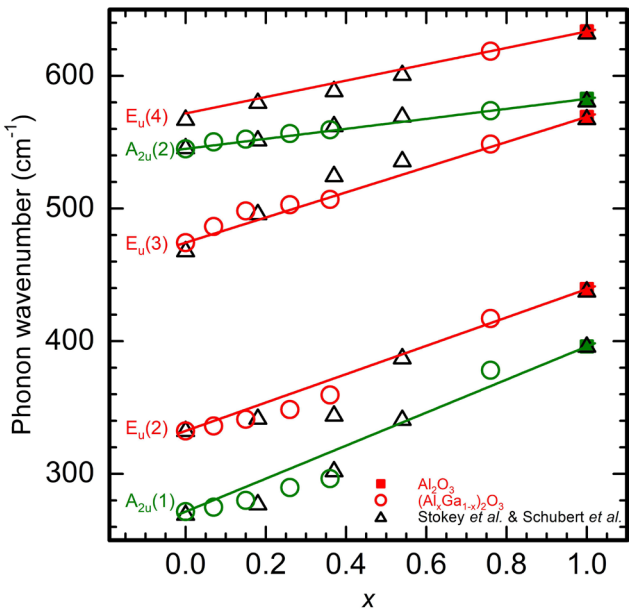

FIG. 4. Phonon wavenumbers (ω_0) of the anisotropic infrared active optical phonon modes with the E_u ($\mathbf{E}\perp\mathbf{c}$) modes in red, and the A_{2u} ($\mathbf{E}||\mathbf{c}$) modes in green in α-$(Al_xGa_{1-x})_2O_3$ for different Al concentrations x, and a m-plane sapphire wafer. In comparison literature data from Stokey *et al.*[46,60] on α-Ga_2O_3 & α-$(Al_xGa_{1-x})_2O_3$ and Schubert *et al.*[61] on Al_2O_3 (black triangles) is displayed as well. The linear interpolations are direct connections from x = 0 to x = 1.

TABLE II. Phonon wavenumbers (ω_0) of the IR active optical phonon modes E_u ($\mathbf{E}\perp\mathbf{c}$) and A_{2u} ($\mathbf{E}||\mathbf{c}$) by infrared spectroscopic ellipsometry for all investigated α-$(Al_xGa_{1-x})_2O_3$ samples and a m-plane sapphire wafer (x=1), along with literature data on c-plane Ga_2O_3,[13,15] m-plane Ga_2O_3,[59,60] and c,- a-, and m-plane Al_2O_3.[13,61] Estimated, not measured, values in the literature are printed *italic*.

x	$E_u(1)$	$E_u(2)$	$E_u(3)$	$E_u(4)$	$A_{2u}(1)$	$A_{2u}(2)$
			cm^{-1}			
0[a]	-	333.7	470.8	567.6	-	-
0[b]	-	333.4	469.9	562.7	*280*	*544*
0[c]	*230*	333.2	474.1	571.7	271.3	546.6
0[d]	221.7	334.0	469.5	568.5	270.8	547.1
0	-	332.4	474.3	-	271.5	545.0
0.07	-	336.1	486.5	-	274.9	550.2
0.15	-	341.2	498.2	-	280.0	552.3
0.26	-	348.5	502.9	-	289.7	556.5
0.36	-	359.5	506.9	-	296.4	559.4
0.76	-	417.1	548.6	618.6	378.1	573.7
1	384.8	439.3	569.1	633.5	396.0	582.7
1[c]	384.8	439.5	569.1	633.4	396.7	582.7
1[e]	385.0	439.1	569.0	633.6	397.5	582.4

[a] Reference [15]
[b] Reference [13]
[c] Reference [59]
[d] Reference [60]
[e] Reference [61]

sults. Hilfiker *et al.*[16,28] obtain a band order $E_{CV,\perp}<E_{CV,||}$ while Kracht *et al.*[14] have the opposite result $E_{CV,\perp} > E_{CV,||}$ (see Fig. 8, bottom panel). The contradiction originates from different approaches used to model the absorption onset and consequently very different exciton binding energies. In Kracht *et al.*[14] 38meV was obtained for excitons related to both absorption onsets by using Elliot's classical theory,[62] while Hilfiker *et al.*[16,28] described excitons as anharmonically broadened Lorentz oscillators. This approach has the advantage of producing ε_1 and ε_2 simultaneously but the disadvantage of negative contributions to absorption curves and very anisotropic exciton binding energies of 10meV ($\perp$) and 180meV ($||$).

No matter how the analysis is performed in detail, we observe very similar transition energies for α-Ga_2O_3 and as well for α-Al_2O_3.[19] Therefore, we expect the same to hold true for the ternary alloy system. Our DFs for ternary α-$(Al_xGa_{1-x})_2O_3$ are very similar in shape and amplitude to the case of α-Ga_2O_3. However, it is increasingly difficult for increasing x to perform a clean Elliot fit due to the fact that our spectral range ends at 6.6eV where the signal is already relatively noisy. Therefore, we use the values from our ear-

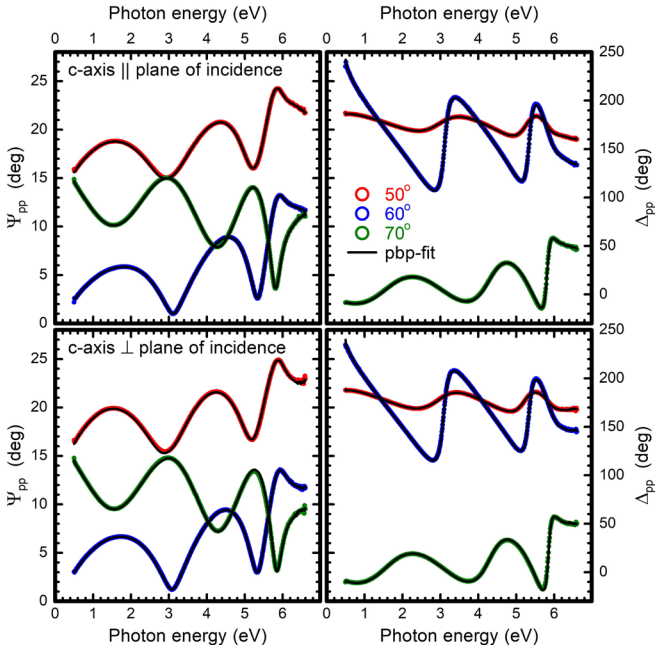

FIG. 5. Ellipsometric angles Ψ_{pp} (Left) and Δ_{pp} (right) of α-$(Al_xGa_{1-x})_2O_3$ for x=0.26 in the visible and ultraviolet spectral range (UV) with the c-axis perpendicular to the plane of incidence (bottom) and parallel to the plane of incidence (top) for three different angles of incidence 50°, 60°, and 70° in red, blue, and green respectively, together with their corresponding point-by-point (pbp) fit in black.

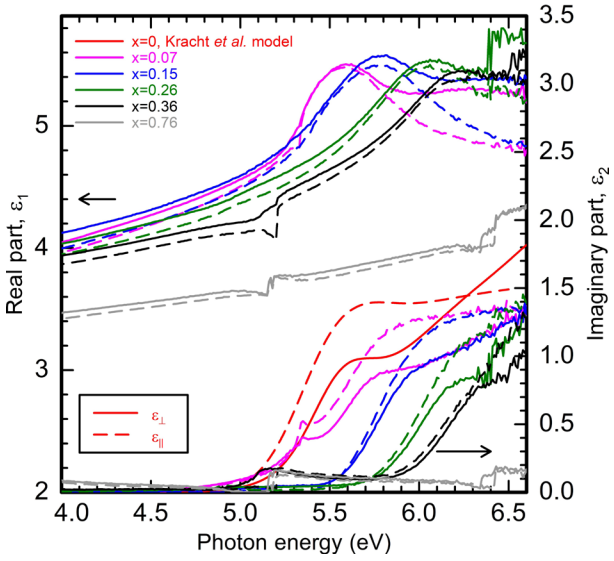

FIG. 6. Point-by-point complex dielectric functions of α-$(Al_xGa_{1-x})_2O_3$ with x between 0.07 and 0.76, with $\varepsilon\perp$ as solid and $\varepsilon\|$ as dashed line, in the ultraviolet (UV) spectral range, supplementedmented by the imaginary part of the model dielectric function of α-Ga_2O_3 by Kracht *et al.*[14]

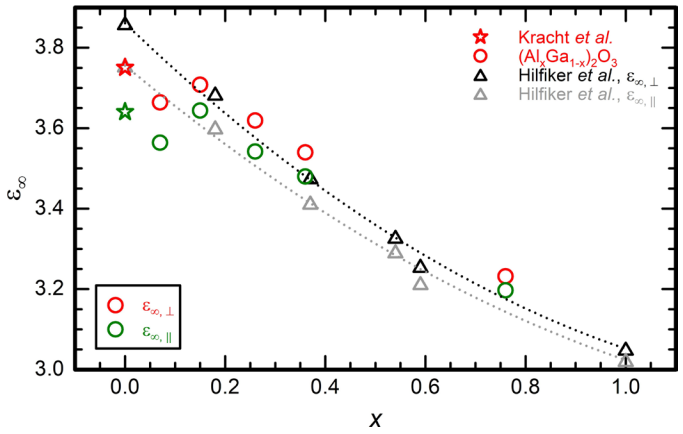

FIG. 7. Anisotropic dielectric limit ε_∞ of α-$(Al_xGa_{1-x})_2O_3$ with x between 0.07 and 0.76 ($\varepsilon_{\infty,\square}$ red, $\varepsilon_{\infty,||}$ green) supplemented by the values for α-Ga_2O_3 by Kracht *et al.*[14] (stars). Additionally, for comparison, data published by Hilfiker *et al.*[45] ($\varepsilon_{\infty,\perp}$,black, $\varepsilon_{\infty,||}$ gray) and the corresponding bowing fits are reproduced as well.

lier result (Kracht *et al.*:14 $E_{CV,\perp}$=5.62eV & $E_{CV,||}$=5.58eV) as fixed parameters and analyze the relative shift on the photon energy axis for increasing x.

To gain the Γ-point transition energies we use a model fit, explained in Sec. II (see also supplement Fig. S2). So obtained results, (values for x=1 i.e. Al_2O_3, are taken from Harman *et al.*:[19] $E_{CV,\square}$ = 9.25eV & $E_{CV,||}$ = 9.2eV) are shown in Fig. 8 (upper panel). Independent bowing fits for $E_{CV,\square}$ and $E_{CV,||}$ yield $b_\square$ = 2.1eV and $b_{||}$ = 1.7eV. Hilfiker *et al.*[28] published $b_\square$= 1.31eV and $b_{||}$= 1.63eV, which differs significantly in the case of the $b_\square$. Also in Fig. 8 we displayed the results of the not-anisotropic study by Bhuiyan *et al.*[47] determined by X-ray Photoelectron Spectroscopy (XPS), leading to b= 2.16eV, close to $b_\square$of this work. It is noticeable that all values by Bhuiyan *et al.*[47] in Fig. 8 are below this work, however the determination by XPS leads to the fundamental, in α-Ga_2O_3 indirect, bandgap, not the fundamental Γ-point transition. Since also Al_2O_3 possibly has an indirect bandgap,[63] based on this results this seems to hold true for the ternary alloy system as well. Thus, unlike Hilfiker *et al.*,[28] we do not expect a change in the direct/indirect nature of the bandgap in α-$(Al_xGa_{1-x})_2O_3$.

IV. SUMMARY

In conclusion, we investigated α-$(Al_xGa_{1-x})_2O_3$thin films grown by metal-organic chemical vapour deposition on m-plane sapphire, anisotropically with x-ray diffraction, infrared (IR) and visible-ultraviolet (UV) spectroscopic ellipsometry. We find the lattice parameters and the anisotropic complex dielectric function (DF) in the IR and UV spectral regions. The IR DF yields the shift of the IR active phonons modes with Al content. A linear shift to higher wavenumbers with increasing x is found, in agreement to literature.[46] An evaluation of the UV DFs using the Shokhovets model[58] yields the dielectric limits ε_∞. The trend in ε_∞ with Al content fits to the earlier results,[45] following a bowing model. Finally, at the onset of strong ab-

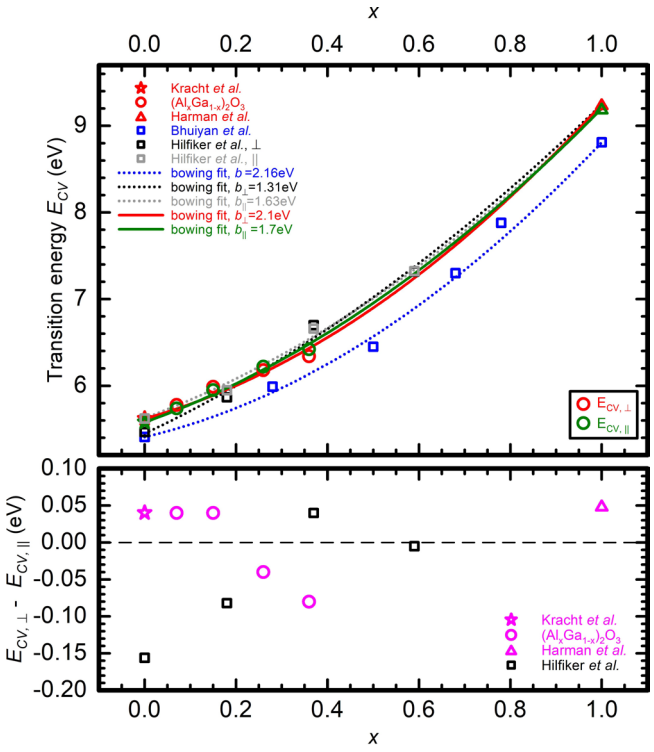

FIG. 8. Γ-Point transition energies E_{CV} with $E_{CV,\perp}$ in red and $E_{CV,||}$ in green of α-$(Al_x Ga_{1-x})_2O_3$ for different Al concentrations, expanded with data for Ga_2O_3 by Kracht *et al.*[14] (stars), Al_2O_3 by Harman *et al.*[19] (triangles) and in comparison to the not anisotropic study from Bhuiyan *et al.*[47] (blue), and the anisotropic one from Hilfiker *et al.*[28] (⊥ black, || gray) in the top panel. Bowing fits (solid lines) are added to determine the bowing parameter *b*. In the bottom panel the difference between $E_{CV,\perp}$ and $E_{CV,||}$ of α-$(Al_x Ga_{1-x})_2O_3$ is displayed for the different Al concentrations (pink circles) along with the corresponding values by Kracht *et al.*[14] (pink star), Harman *et al.*[19] (pink triangle), and Hilfiker *et al.*[28] (black squares).

sorption we find the Γ-point transition energies. A strong increase, with increasing *x*, also in accordance with a bowing model, is shown. We determine anisotropic bowing parameters of $b_\perp$ = 2.1eV and $b_{||}$ = 1.7eV.

SUPPLEMENT

See the supplementary material for a comparison of the UV point-by-point (pbp) dielectric functions (DFs) in the region of photon energies lower than the absorption onset and their corresponding Shokhovets-fit, used to determine the dielectric limit ε_∞. Also displayed is a comparison of the UV pbp-DFs and the corresponding model DFs used to extract the Γ-point transition energies displayed in Fig. 8.

ACKNOWLEDGMENTS

This work was funded in part by the Leibniz Science Campus GraFOx II. Bhuiyan, Meng, and Zhao acknowledge funding support from the US Department of Defense, Air Force Office of Scientific Research GAME MURI Program (grant# FA9550-18-1-0479) and from US NSF (grant# 2019753 and 2231026).

DATA AVAILABILITY

The data that support the findings of this study are available from the corresponding author upon reasonable request.

[1] J. A. Spencer, A. L. Mock, A. G. Jacobs, M. Schubert, Y. Zhang, and M. J. Tadjer, Applied Physics Reviews **9**, 011315 (2022).
[2] X. Hou, Y. Zou, M. Ding, Y. Qin, Z. Zhang, X. Ma, P. Tan, S. Yu, X. Zhou, X. Zhao, et al., Journal of Physics D: Applied Physics **54**, 043001 (2020).
[3] O. Slobodyan, J. Flicker, J. Dickerson, J. Shoemaker, A. Binder, T. Smith, S. Goodnick, R. Kaplar, and M. Hollis, Journal of Materials Research **37**, 849 (2022).
[4] B. R. Tak, S. Kumar, A. K. Kapoor, D. Wang, X. Li, H. Sun, and R. Singh, Journal of Physics D: Applied Physics **54**, 453002 (2021).
[5] S. J. Pearton, J. Yang, P. H. Cary, F. Ren, J. Kim, M. J. Tadjer, and M. A. Mastro, Applied Physics Reviews **5**, 011301 (2018).
[6] M. Higashiwaki, K. Sasaki, H. Murakami, Y. Kumagai, A. Koukitu, A. Kuramata, T. Masui, and S. Yamakoshi, Semiconductor Science and Technology **31**, 034001 (2016).
[7] D. Guo, Q. Guo, Z. Chen, Z. Wu, P. Li, and W. Tang, Materials Today Physics **11**, 100157 (2019).
[8] L. K. Ping, D. D. Berhanuddin, A. K. Mondal, P. S. Menon, and M. A. Mohamed, Chinese Journal of Physics **73**, 195 (2021).
[9] T. Minami, Y. Nishi, and T. Miyata, Applied Physics Express **6**, 04410 (2013).
[10] T. Minami, Y. Nishi, and T. Miyata, Applied Physics Express **8**, 022301 (2015).
[11] L. E. Ratcliff, T. Oshima, F. Nippert, B. M. Janzen, E. Kluth, R. Goldhahn, M. Feneberg, P. Mazzolini, O. Bierwagen, C. Wouters, et al., Advanced Materials **34**, 2204217 (2022).
[12] J. Furthmüller and F. Bechstedt, Phys. Rev. B **93**, 115204 (2016).
[13] M. Feneberg, J. Nixdorf, M. D. Neumann, N. Esser, L. Artús, R. Cuscó, T. Yamaguchi, and R. Goldhahn, Phys. Rev. Materials **2**, 044601 (2018).
[14] M. Kracht, A. Karg, M. Feneberg, J. Bläsing, J. Schörmann, R. Goldhahn, and M. Eickhoff, Phys. Rev. Applied **10**, 024047 (2018).
[15] P. Ning, J. Grümbel, J. Bläsing, R. Goldhahn, D.-W. Jeon, and M. Feneberg, Semiconductor Science and Technology **35**, 095001 (2020).
[16] M. Hilfiker, R. Korlacki, R. Jinno, Y. Cho, H. G. Xing, D. Jena, U. Kilic, M. Stokey, and M. Schubert, Applied Physics Letters **118**, 062103 (2021).
[17] O. Bierwagen, Semiconductor Science and Technology **30**, 024001 (2015).
[18] R. Cuscó, T. Yamaguchi, E. Kluth, R. Goldhahn, and M. Feneberg, Applied Physics Letters **121**, 062106 (2022).
[19] A. K. Harman, S. Ninomiya, and S. Adachi, Journal of Applied Physics **76**, 8032 (1994).
[20] M. Feneberg, M. F. Romero, M. Röppischer, C. Cobet, N. Esser, B. Neuschl, K. Thonke, M. Bickermann, and R. Goldhahn, Phys. Rev. B **87**, 235209 (2013).
[21] Y.-F. Wu, D. Kapolnek, J. Ibbetson, P. Parikh, B. Keller, and U. Mishra, IEEE Transactions on Electron Devices **48**, 586 (2001).
[22] I. Akasaki, H. Amano, S. Sota, H. Sakai, T. Tanaka, and M. Koike, Japanese Journal of Applied Physics **34**, L1517 (1995).
[23] S. Nakamura, M. Senoh, S. ichi Nagahama, N. Iwasa, T. Yamada, T. Matsushita, H. Kiyoku, and Y. Sugimoto, Japanese Journal of Applied Physics **35**, L74 (1996).
[24] Q. Cai, H. You, H. Guo, J. Wang, B. Liu, Z. Xie, D. Chen, H. Lu, Y. Zheng, and R. Zhang, Light: Science & Applications **10**, 94 (2021).

[25]V. G. Hill, R. Roy, and E. F. Osborn, Journal of the American Ceramic Society **35**, 135 (1952).
[26]A. Mauze and J. Speck, *Plasma-Assisted Molecular Beam Epitaxy 1* (Springer International Publishing, Cham, 2020), pp. 79–9
[27]M. Hilfiker, U. Kilic, A. Mock, V. Darakchieva, S. Knight, R. Korlacki,
A. Mauze, Y. Zhang, J. Speck, and M. Schubert, Applied Physics Letters **114**, 231901 (2019).
[28]M. Hilfiker, U. Kilic, M. Stokey, R. Jinno, Y. Cho, H. G. Xing, D. Jena, R. Korlacki, and M. Schubert, Applied Physics Letters **121**, 052101 (2022).
[29]G. T. Dang, T. Yasuoka, Y. Tagashira, T. Tadokoro, W. Theiss, and T. Kawaharamura, Applied Physics Letters **113**, 062102 (2018).
[30]Z. Chen, M. Arita, K. Saito, T. Tanaka, and Q. Guo, AIP Advances **11**, 035319 (2021).
[31]R. Kumaran, T. Tiedje, S. E. Webster, S. Penson, and W. Li, Opt. Lett. **35**, 3793 (2010).
[32]R. Jinno, C. S. Chang, T. Onuma, Y. Cho, S.-T. Ho, D. Rowe, M. C. Cao, K. Lee, V. Protasenko, D. G. Schlom, et al., Science Advances **7**, eabd5891 (2021).
[33]R. Schewski, G. Wagner, M. Baldini, D. Gogova, Z. Galazka, T. Schulz, T. Remmele, T. Markurt, H. von Wenckstern, M. Grundmann, et al., Applied Physics Express **8**, 011101 (2014).
[34]Z. Cheng, M. Hanke, P. Vogt, O. Bierwagen, and A. Trampert, Applied Physics Letters **111**, 162104 (2017).
[35]H. Y. Kang, Y. Choi, K. Pyeon, T. H. Lee, and R. B. K. Chung, Journal of Materials Science **57**, 19882 (2022).
[36]A. Y. Polyakov, N. B. Smirnov, I. V. Shchemerov, E. B. Yakimov, V. I. Nikolaev, S. I. Stepanov, A. I. Pechnikov, A. V. Chernykh, K. D. Shcherbachev, A. S. Shikoh, et al., APL Materials **7**, 051103 (2019).
[37]H. Okumura, Japanese Journal of Applied Physics **61**, 125505 (2022).
[38]G. T. Dang, Y. Tagashira, T. Yasuoka, L. Liu, and T. Kawaharamura, AIP Advances **10**, 115019 (2020).
[39]K. Akaiwa, K. Ota, T. Sekiyama, T. Abe, T. Shinohe, and K. Ichino, physica status solidi (a) **217**, 1900632 (2020).
[40]S. Mu and C. G. Van de Walle, Phys. Rev. Materials **6**, 104601 (2022).
[41]D. Wickramaratne, J. B. Varley, and J. L. Lyons, Applied Physics Letters **121**, 042110 (2022).
[42]H. Ito, K. Kaneko, and S. Fujita, Japanese Journal of Applied Physics **51**, 100207 (2012).
[43]T. Uchida, R. Jinno, S. Takemoto, K. Kaneko, and S. Fujita, Japanese Journal of Applied Physics **57**, 040314 (2018).
[44]X. Xia, C. Fares, F. Ren, A. Hassa, H. von Wenckstern, M. Grundmann, and S. J. Pearton, ECS Journal of Solid State Science and Technology **10**, 113007 (2021).
[45]M. Hilfiker, U. Kilic, M. Stokey, R. Jinno, Y. Cho, H. G. Xing, D. Jena, R. Korlacki, and M. Schubert, Applied Physics Letters **119**, 092103 (2021).
[46]M. Stokey, T. Gramer, R. Korlacki, S. Knight, S. Richter, R. Jinno, Y. Cho, H. G. Xing, D. Jena, M. Hilfiker, et al., Applied Physics Letters **120**, 112202 (2022).
[47]A. F. M. A. U. Bhuiyan, Z. Feng, H.-L. Huang, L. Meng, J. Hwang, and H. Zhao, APL Materials **9**, 101109 (2021).
[48]M. Marezio and J. P. Remeika, The Journal of Chemical Physics **46**, 1862 (1967).
[49]M. Leszczynski, T. Suski, H. Teisseyre, P. Perlin, I. Grzegory, J. Jun, S. Porowski, and T. D. Moustakas, Journal of Applied Physics **76**, 4909 (1994).
[50]L. Vegard, Zeitschrift für Physik **5**, 17 (1921).
[51]M. Schubert, B. Rheinländer, J. A. Woollam, B. Johs, and C. M. Herzinger, J. Opt. Soc. Am. A **13**, 875 (1996).
[52]M. Feneberg, C. Lidig, K. Lange, M. E. White, M. Y. Tsai, J. S. Speck, O. Bierwagen, and R. Goldhahn, physica status solidi (a) **211**, 82 (2014).
[53]R. Cuscó, N. Domènech-Amador, T. Hatakeyama, T. Yamaguchi, T. Honda, and L. Artús, Journal of Applied Physics **117**, 185706 (2015).
[54]D. A. G. Bruggeman, Annalen der Physik **421**, 160 (1937).
[55]I. H. Malitson, J. Opt. Soc. Am. **52**, 1377 (1962).
[56]*Guide to Using WVASE 32: Spectroscopic Ellipsometry Data Acquisition and Analysis Software* (J. A. Woollam Company, Incorporated, 2008).
[57]C. M. Herzinger and B. D. Johs, *Dielectric function parametric model, and method of use*, U.S. Patent 5796983 (1998).
[58]S. Shokhovets, R. Goldhahn, G. Gobsch, S. Piekh, R. Lantier, A. Rizzi, I. Lebedev, and W. Richter, Journal of Applied Physics **94**, 307 (2003).
[59]M. Feneberg, J. Bläsing, T. Sekiyama, K. Ota, K. Akaiwa, K. Ichino, and R. Goldhahn, Applied Physics Letters **114**, 142102 (2019).
[60]M. Stokey, R. Korlacki, M. Hilfiker, S. Knight, S. Richter, V. Darakchieva, R. Jinno, Y. Cho, H. G. Xing, D. Jena, et al., Phys. Rev. Mater. **6**, 014601 (2022).
[61]M. Schubert, T. E. Tiwald, and C. M. Herzinger, Phys. Rev. B **61**, 8187 (2000).
[62]R. J. Elliott, Phys. Rev. **108**, 1384 (1957).
[63]R. Santos, E. Longhinotti, V. Freire, R. Reimberg, and E. Caetano, Chemical Physics Letters **637**, 172 (2015)